



# Porous BN/TiO<sub>2</sub> hybrid nanosheets as highly efficient visible-light-driven photocatalysts

Dan Liu<sup>a,1</sup>, Mingwen Zhang<sup>a,1</sup>, Wanjie Xie<sup>a</sup>, Lu Sun<sup>a,b</sup>, Ying Chen<sup>a,\*</sup>, Weiwei Lei<sup>a,\*</sup>

<sup>a</sup> Institute for Frontier Materials, Deakin University, Victoria 3216, Australia

<sup>b</sup> School of Textile Science and Engineering, Wuhan Textile University, Wuhan 430073, China

## ARTICLE INFO

### Article history:

Received 8 November 2016

Received in revised form 17 January 2017

Accepted 4 February 2017

Available online 6 February 2017

### Keywords:

Porous BN/TiO<sub>2</sub> hybrid nanosheets

Visible light

Organic pollutants degradation

Excellent recyclability

## ABSTRACT

Porous boron nitride (BN) nanosheets, which possess extreme large surface areas, high thermal conductivity and special chemical activities, have demonstrated advantages in water cleaning and energy storage. However, they are usually considered as an underachieving catalytic material for photocatalysis and other photovoltaic conversion applications due to their wide band gap of 5.5 eV. Here, we report a novel porous BN/TiO<sub>2</sub> hybrid nanosheets with the formation of new B—O—Ti bondings between the boron dangling bonds at the open edges of pores of porous BN nanosheets and nanosized TiO<sub>2</sub> particles. Such highly active bondings make the hybrid nanosheets responsive to an extended wavelength range from UV to visible light ( $\lambda > 420$  nm) spectrum and also substantially enhance the photocatalytic effect (up to 99%) for degradation of organic molecules. In addition, the porous BN/TiO<sub>2</sub> hybrid nanosheets exhibit excellent cycling stability up to 5 cycles maintaining high visible-light photocatalytic activity (97%). These results provide new insights for design of advanced hybrid photocatalysts with actively chemical bonding species, which can be applied in environmental protection, water splitting, and photo-electrochemical conversion.

© 2017 Elsevier B.V. All rights reserved.

## 1. Introduction

Porous two-dimensional (2D) nanomaterials with unique structural advantages have led to their intriguing properties, attractive applications, as well as industrial and environmental benefits [1–4]. Several porous 2D nanomaterials, including ZnO nanosheets [5], In<sub>2</sub>O<sub>3</sub> nanosheets [6], graphene [7], and BN nanosheets [4] were successfully produced and they exhibit significantly new properties in oil adsorption, gas sensing, biological probes, water cleaning, and electrochemical energy storage and conversion. One of the most attractive functionalities of the porous 2D nanomaterials is that they can interact with various organic or inorganic species not only on the surfaces but also at the edges of pores due to a large number of exposed and active radicals [8–10]. Therefore, the design and fabrication of unconventional porous nanosheet structures with highly active edges is an appealing endeavor for new properties and applications.

Among various 2D nanomaterials, boron nitride nanosheets (BNNSs), so-called “white graphene” due to the similarity to graphene, consist of a honeycomb structure of covalently bound boron and nitrogen atoms [11]. It has unique electronic features with a wide bandgap of up to 5.5 eV, and some important applications such as a deep-ultraviolet-light emitter and perfect substrates for graphene based devices [12,13]. Although BNNSs are not commonly considered as a catalytic material for photocatalysis and other photovoltaic conversion applications because of the strong optical absorption within the ultraviolet-visible region, they could be a promising support material for catalysts due to its remarkable properties, including extremely high resistance to oxidation and good chemical inertness, high thermal conductivity, high melting point and high surface area, especially under relatively harsh conditions, as it could avoid the sintering of the supported catalysts on hot spots [14–20]. Besides of the intrinsic properties of BNNSs, porous BNNSs with plentiful pores and large surface areas are showing some innovative applications in hydrogen storage and water cleaning treatment [21–26].

In this work, we demonstrated a rationally design of porous BN/TiO<sub>2</sub> hybrid nanosheets with a large number of new B—O—Ti chemical bonds. The synthesized porous BN/TiO<sub>2</sub> hybrid nanosheets possess much higher photocatalytic activity and regeneration ability for degradation of organic molecules in both UV and

\* Corresponding authors.

E-mail addresses: [ian.chen@deakin.edu.au](mailto:ian.chen@deakin.edu.au) (Y. Chen), [weiwei.lei@deakin.edu.au](mailto:weiwei.lei@deakin.edu.au) (W. Lei).

<sup>1</sup> These authors contributed equally.

visible light ( $\lambda > 420$  nm). A mechanism on their highly efficient visible-light-driven characteristic was also proposed based on the experimental results. All the results implicated the great potentials of the developed porous BN/TiO<sub>2</sub> hybrid nanosheets and inspired the further design of the BN-based photocatalytic materials.

## 2. Experimental

### 2.1. Synthesis of samples

Porous boron nitride nanosheets were produced by a dynamic templating approach using boron trioxide and guanidine hydrochloride [4]. In a typical experimental run, boron trioxide and guanidine hydrochloride with 1:5 molar ratio were mixed in 10 mL methanol under stirring to form a clear, colorless solution. After 24 h fast stirring, a white crystalline powder (a complex between the boron trioxide and guanidine chloride) as precursors was formed. After that, the precursors were put into a quartz boat and then heated at a rate of 10 °C/min and kept at 1100 °C for 2 h under nitrogen/hydrogen (15% hydrogen) gas flow. Finally, the sample was obtained. Non-porous boron nitride nanosheets (NP-BNNSSs) were described as elsewhere [27]. Typically, boric acid and urea were mixed at a molar ratio of 1:48, followed by being added with distilled water (40 mL) and heated at 65 °C until the water was fully evaporated. The mixture was then heated at 900 °C in a N<sub>2</sub> atmosphere for 5 h to obtain white products.

Commercial P25 (80% anatase and 20% rutile TiO<sub>2</sub>, 21 nm particle size) were purchased from Sigma-Aldrich (Australia). TiO<sub>2</sub> precursor solution was used as the starting material and prepared by the following route. In a typical run, 1 mL of tetrabutyl titanate (TBT, Ti(OC<sub>4</sub>H<sub>9</sub>)<sub>4</sub> from Sigma-Aldrich) was dissolved in 5 mL of ethanol using ultrasonic vibration for 5 min, to form a transparent solution. Then 2 mL nitric acid (HNO<sub>3</sub>, 73 wt.%) was added drop wise into the ethanol solution with vigorous stirring. The obtained solution was further diluted to 10 mL by ethanol to form a clear TiO<sub>2</sub> precursor.

40 mg porous BNNSSs was first dispersed in 20 mL nitric acid (8 M) under ultrasonic treatment for 2 h at room temperature, and then the treated porous BNNSSs was obtained after washing repeatedly with ethanol and separating by centrifugation. The treated porous BNNSSs was dispersed into 20 mL ethanol by ultrasonic vibration for 10 min, then TiO<sub>2</sub> precursor solution was added into the dispersion under vigorous stirring. After stirring for 30 min, the obtained dispersion was further diluted to 25 mL by ethanol and transferred to a 50 mL stain steel autoclave. The thermal recrystallization treatments were carried out at 180 °C for 20 h. After that, the autoclave was allowed to cool down naturally. Brown precipitates of porous BN/TiO<sub>2</sub> hybrid nanosheets were collected and washed with ethanol three times to remove impurities. Finally, the precipitates were dried at room temperature overnight. The TiO<sub>2</sub> nanoparticles and porous BN/TiO<sub>2</sub> hybrid nanosheets with different ratio of TiO<sub>2</sub> were prepared using the same method. 40 mg of porous BNNSSs was added to the calculated amount of the above reaction system to prepare 18 wt%, 38 wt% and 51 wt% porous BN/TiO<sub>2</sub> hybrid nanosheets catalysts with different weight addition ratios of TiO<sub>2</sub> in porous BN/TiO<sub>2</sub> hybrid nanosheets. 18 wt%, 38 wt% and 51 wt% were the weight of TiO<sub>2</sub> over that of porous BN/TiO<sub>2</sub> nanosheets. Similar to the preparation method for porous BN/TiO<sub>2</sub> hybrid nanosheets, non-porous BN/TiO<sub>2</sub> hybrid nanosheets were obtained by replacing porous BNNSSs with non-porous BNNSSs.

### 2.2. Materials characterization

The crystallite structures were determined on a Panalytical X'Pert PRO X-ray powder diffraction (XRD) using Cu K $\alpha$  radiation in a 2 $\theta$  range from 15° to 80° at room temperature. Fourier trans-

form infrared spectroscopy (FTIR) data were determined from a Bruker FTIR Spectrophotometer in transmission mode, with accumulation of 32 scans at 4 cm<sup>-1</sup> resolution. Transmission electron microscopy (TEM) was performed on a JEOL 2100F high resolution mode operating at 110 kV apparatus. The surface areas of samples were determined from nitrogen adsorption and desorption isotherms using a Tristar 3000 apparatus at 77 K.

### 2.3. Photocatalytic experiments

The photocatalytic activities of products were evaluated of the degradation of rhodamine B (RhB) under simulated solar and visible light ( $\lambda > 420$  nm) irradiation, respectively. In a typical procedure for RhB photocatalytic reaction, the weight of TiO<sub>2</sub> content in different photocatalysts (commercial P25, synthesized TiO<sub>2</sub> nanoparticles, and porous BN/TiO<sub>2</sub> hybrid nanosheets) used for each experiment was kept at 5 mg. The photocatalyst were added into a 100 mL quartz photo-reactor containing 50 mL RhB solution (150 mg L<sup>-1</sup>) for simulated solar light irradiation. The suspension was first ultrasonicated for 10 min, and then stirred in the dark for 1 h to ensure absorption–desorption equilibrium. Subsequently, it was irradiated under the simulated solar light using an Atlas Suntest CPS1 instrument (Ametek, United States) equipped with 1500 W air cooled xenon arc lamp (light range 300–800 nm wavelengths). The suspensions were stirred constantly during the photocatalytic processes to ensure the uniform dispersion of porous BN/TiO<sub>2</sub> hybrid nanosheets. Filter B was chosen, the temperature inside the box was 35 °C, and the dose was 350 W/m<sup>2</sup>.

For visible light-induced photocatalytic activity tests, both RhB and phenol degradations were carried out by adding the RhB (50 mg L<sup>-1</sup>) and phenol (30 mg L<sup>-1</sup>) solutions with the porous BN/TiO<sub>2</sub> nanosheets (38 wt%), followed by irradiating the suspensions in the same solar simulator through a GG420 cutting filter. The RhB and phenol concentrations were indicated by the absorbance at 554 nm and 269 nm, respectively. The change of their concentrations under simulated visible light irradiation could be used as a measure of the photocatalytic activity. At the given time intervals, 3 mL of the suspension was extracted and then centrifuged to separate the photocatalysts from the supernatant solution. UV-vis absorption spectra of the supernatant was measured using the Varian Cary 3E UV/Vis spectrophotometer. Commercial P25 was also applied in the same conditions for the comparison with porous BN/TiO<sub>2</sub> hybrid nanosheets (38 wt%). TiO<sub>2</sub> content in both porous BN/TiO<sub>2</sub> hybrid nanosheets and commercial P25 was kept at 5 mg and 7.6 mg for RhB and phenol degradation, respectively.

### 2.4. Photocurrent measurements

The photocurrents were measured using an electrochemical workstation (Solartron 1470E) in a standard three electrode system with as-prepared samples (synthesized TiO<sub>2</sub> and porous BN/TiO<sub>2</sub> hybrid nanosheets (38 wt%)) deposited on 1 cm × 1 cm ITO substrate as the working electrode, a Ag/AgCl electrode as reference, and a Pt wire parallel to the working electrode as a counter electrode. The light source employed was a Newport 300W xenon light source, controlled by a Newport Digital Exposure Controller, which simulates the solar light.

### 2.5. Photo-induced chemiluminescence measurements

To compare the free radical populations and decay rates following irradiation on synthesized TiO<sub>2</sub> (6 mg) and porous BN/TiO<sub>2</sub> hybrid nanosheets (38 wt%) (6 mg), a Lumipol 3 chemiluminescence instrument (Polymer Institute, Slovak Academy of Sciences, Bratislava), modified to allow *in situ* irradiation with selected wavelengths from a medium-pressure mercury arc (Lumatec SUV-

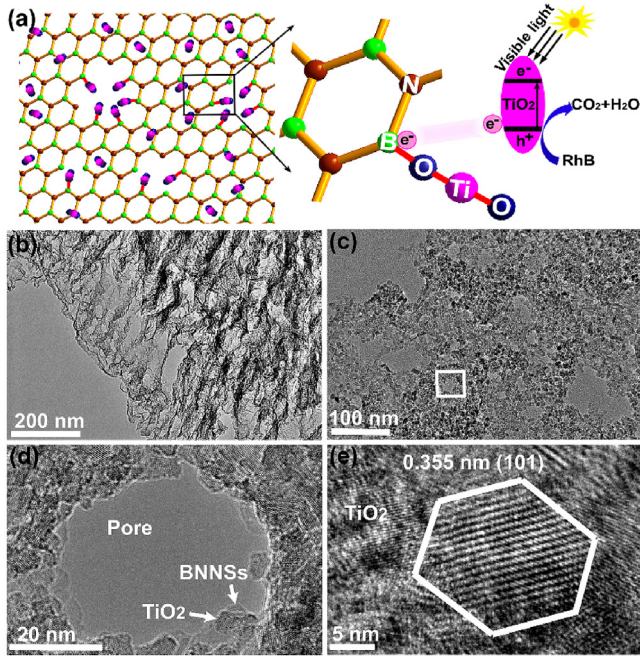


**Fig. 1.** (a) Schematic diagram for the photocatalytic reaction of rhodamine B by porous BN/TiO<sub>2</sub> hybrid nanosheets with new chemical bonding specie B—O—Ti under simulated visible light. TEM images for (b) starting porous BNNSs and (c) porous BN/TiO<sub>2</sub> hybrid nanosheets (TiO<sub>2</sub>: 38 wt%), showing a uniform distribution of TiO<sub>2</sub> nanoparticles on the BNNS surface. (d) and (e) HRTEM images for a hole decorated by TiO<sub>2</sub> nanoparticles from the rectangular area in (c), and a single TiO<sub>2</sub> particle as indicated by the white arrow in (d).

DC, Lumatech GmbH, Germany) under a controlled atmosphere at constant temperature was used. The luminescence baseline was stabilized by equilibrating the sample in nitrogen using a gas flow rate of 200 cm<sup>3</sup>/min and a constant temperature of 40 °C for 1 min. Then the sample was irradiated in N<sub>2</sub> for 2 min with selected wavelengths (320–500 nm) and after a further 2 min the gas flow was switched from N<sub>2</sub> to O<sub>2</sub>, resulting in photo-induced chemiluminescence emission.

### 3. Results and discussions

#### 3.1. Characterizations of porous BN/TiO<sub>2</sub> hybrid nanosheets

The porous BNNSs were produced using a dynamic templating approach with boron trioxide and guanidine hydrochloride as the starting materials and N<sub>2</sub>/H<sub>2</sub> gas as nitrogen source [4]. The TEM and high-resolution TEM (HRTEM) images of as-prepared porous BNNSs are shown in Figs. 1 b and S1, respectively. One can see clearly that porous BNNSs have a layer structure composed of several stacking layers with a large number of pores with diameters ranging from 20 nm to several hundred nanometers. Porous BN/TiO<sub>2</sub> hybrid nanosheets were synthesized using porous BNNSs and tetrabutyl titanate (TBT) as reactants. Different weight percents of TiO<sub>2</sub> were controlled using different amount of TiO<sub>2</sub> precursor solution. As a result, three porous BN/TiO<sub>2</sub> hybrid nanosheets with TiO<sub>2</sub> weight contents of 18 ± 2 wt%, 38 ± 2 wt%, and 51 ± 1 wt% were prepared. The TEM image of porous BN/TiO<sub>2</sub> (38 wt%) hybrid nanosheets (Fig. 1c) shows that the TiO<sub>2</sub> nanoparticles were loaded homogeneously on porous BNNSs, where the TiO<sub>2</sub> nanoparticles with uniform crystallite size of 7–15 nm were densely anchored onto the porous BNNSs. The HRTEM image of porous BN/TiO<sub>2</sub> hybrid nanosheets (38 wt%) shows numerous TiO<sub>2</sub> nanoparticles were densely deposited onto the edge area of pores (Fig. 1d). The HRTEM image of TiO<sub>2</sub> nanoparticles (Fig. 1e) indicates a well-defined crys-

tallinity of TiO<sub>2</sub> with lattice spacing of 0.355 nm, which corresponds to the (101) planes of anatase phase. In the porous BN/TiO<sub>2</sub> hybrid nanosheets of BN/TiO<sub>2</sub> (18 wt%) and BN/TiO<sub>2</sub> (51 wt%), the porous BNNSs are decorated lightly and heavily with TiO<sub>2</sub> nanoparticles, respectively, as shown in Figs. S2 and S3. The homogenous distribution of TiO<sub>2</sub> particles, high porosity and few-layer structure of porous BNNSs benefit to the photocatalytic property.

The structure of samples were investigated by X-ray diffraction (XRD) and XRD patterns are shown in Fig. 2a. Two characteristic diffraction peaks can be observed at 25.6° and 42.5° on the spectra, corresponding to the (002) and (100) planes of h-BN phase, respectively. For synthesized TiO<sub>2</sub> particles, all diffraction peaks can be indexed to anatase TiO<sub>2</sub> crystals (JCPDS No. 21-1272). In the XRD pattern of porous BN/TiO<sub>2</sub> hybrid nanosheets (18 wt%), it can be seen clearly that all the diffraction peaks belong to porous BNNSs and TiO<sub>2</sub>. With the increase of TiO<sub>2</sub> loading amount, the diffraction peak from porous BNNSs is invisible due to its surface covered by TiO<sub>2</sub> particles, as confirmed by TEM images (Fig. S2 and S3). No other diffraction peaks are observed in all the patterns. Fig. 2b displays UV-vis absorption spectra of synthesized TiO<sub>2</sub> and porous BN/TiO<sub>2</sub> hybrid nanosheets with different TiO<sub>2</sub> loading. The porous BN/TiO<sub>2</sub> hybrid nanosheets exhibit increased absorption in the visible light region, compared to synthesized TiO<sub>2</sub>. Particularly, one can see that the porous BN/TiO<sub>2</sub> hybrid nanosheets (38 wt%), which showed the best photocatalytic performance as discussed below, exhibited a much stronger tailing adsorption covering the whole visible light region than the synthesized TiO<sub>2</sub>, suggesting the excellent visible light harvesting behavior of the porous BN/TiO<sub>2</sub> hybrid nanosheets (38 wt%). The inset in Fig. 2b shows the plots of Kubelka-Munk remission function [28] (i.e., relationship of [F(R)Eg]<sup>1/2</sup> versus photon energy (Eg = hν)) corresponding to the spectrum of synthesized TiO<sub>2</sub> particles and porous BN/TiO<sub>2</sub> (38 wt%) hybrid nanosheets, which indicates that the band gap of synthesized TiO<sub>2</sub> was 3.13 ± 0.02 eV while the band gap of the porous BN/TiO<sub>2</sub> (38 wt%) was significantly reduced to 2.95 ± 0.03 eV. In addition, it is well known that BN has a wide band gap of 5.5 eV and thus has no any optical absorption in a wavelength higher than 350 nm (Fig. S4). Therefore, the significant reduction of the band gap of porous BN/TiO<sub>2</sub> hybrid nanosheets, compared with synthesized TiO<sub>2</sub>, suggests a rearrangement of the energy levels of TiO<sub>2</sub> by forming B—O—Ti bonds after its incorporation into porous BNNSs.

The N<sub>2</sub> adsorption–desorption isotherms were conducted to determine the specific surface area of the porous BN/TiO<sub>2</sub> hybrid nanosheets (38 wt%). The isotherms are a characteristic of type II isotherms with a hysteresis loop at a relative pressure between 0.4 and 1.0, which reveals predominant a mesoporous structure, as shown in Fig. S5. Calculation with the BET and BJH models gives a specific surface area of 263 m<sup>2</sup> g<sup>-1</sup> and the total pore volumes 0.26 cm<sup>3</sup> g<sup>-1</sup>, respectively, indicating a relatively high surface area in the porous BN/TiO<sub>2</sub> hybrid nanosheets (38 wt%). Such high surface area increases the charge transfer rate of electrons and surface-adsorbed amount of chemical molecules through π–π interactions [29].

The interaction between porous BNNSs and TiO<sub>2</sub> in porous BN/TiO<sub>2</sub> hybrid nanosheets (38 wt%) was investigated using X-ray photoelectron spectroscopy (XPS) analysis. Besides the standard sp<sup>2</sup>-hybridized BN structures in both porous BNNSs and porous BN/TiO<sub>2</sub> hybrid nanosheets (38 wt%) (in Fig. 2c), the shoulder peaks with different relative intensities located at the binding energy of 191.7 and 192.2 eV in B1s spectra are attributed to the edge or interfacial B dangling bonds linked with —OH and —OTi groups, respectively [30]. To compare with porous BNNSs and its TiO<sub>2</sub> hybrid nanosheets (38 wt%), we have synthesized non-porous BNNSs and its TiO<sub>2</sub> hybrid nanosheets (TiO<sub>2</sub>: 38 wt%) following the preparation method for non-porous BNNSs in the reference [27].

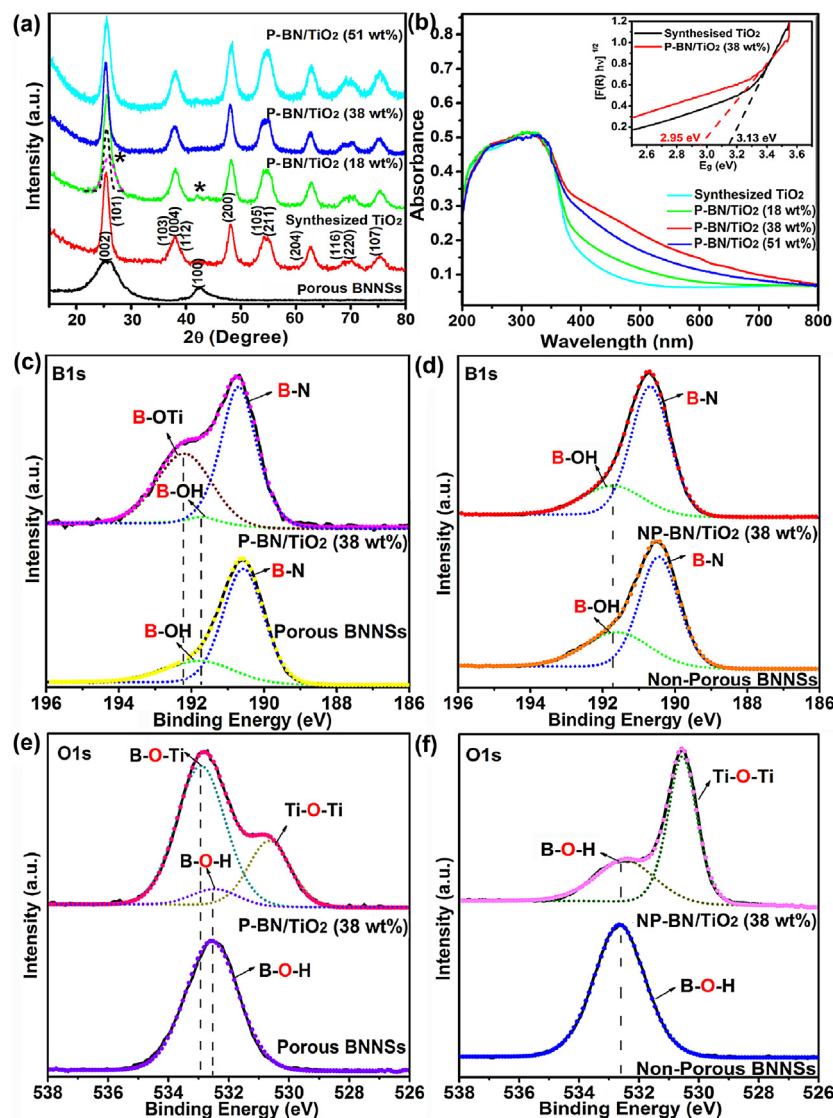


**Fig. 2.** (a) XRD patterns of porous BNNs, synthesized TiO<sub>2</sub>, and porous BN/TiO<sub>2</sub> hybrid nanosheets with different loading amount of TiO<sub>2</sub> nanoparticles. (b) UV-vis absorption spectra of synthesized TiO<sub>2</sub> and different porous BN/TiO<sub>2</sub> hybrid nanosheets (for comparison). The inset figure shows the relationship between the transformed Kubelka-Munk function versus the light energy for synthesized TiO<sub>2</sub> and porous BN/TiO<sub>2</sub> (38 wt%) hybrid nanosheets. XPS spectra of porous and non-porous BNN samples, porous and non-porous BN/TiO<sub>2</sub> hybrid nanosheets (38 wt%). (c) and (d) B1s, (e) and (f) O1s.

In contrast, non-porous BNNs don't show any pores on the surface inducing a relative low surface area [4,27]. In addition, the binding energy of non-porous BN/TiO<sub>2</sub> hybrid nanosheets (TiO<sub>2</sub>: 38 wt%) was further studied by XPS. The peak positions of binding energy in B1s spectra does not shift for TiO<sub>2</sub> in non-porous BN/TiO<sub>2</sub> hybrid nanosheets (38 wt%) (Fig. 2c and d), indicating no formation of B—O—Ti bonds in non-porous BN/TiO<sub>2</sub> hybrid nanosheets. The formation of B—O—Ti bonds in porous BN/TiO<sub>2</sub> hybrid nanosheets (38 wt%) can be further examined and confirmed by the analysis of O1s spectra, as shown in Fig. 2e. The peak located at binding energy of 532.5 eV is assigned to the B—O—H bonds relating to surface hydroxyl groups on both porous and non-porous BNNs. The O1s region of porous BN/TiO<sub>2</sub> hybrid nanosheets (38 wt%) could be composed of three different species. The first peak at 530.6 eV corresponds to O—Ti bond of TiO<sub>2</sub> phase. Compared with porous BNNs, the B—O—H peak in O1s region at 532.5 eV of porous BN/TiO<sub>2</sub> hybrid nanosheets (38 wt%) is too weak to be discernible. On the contrary, the strongest peak at 532.9 eV is observed, which is assigned to the formation of a chemical B—O—Ti bond between a titanium atom of TiO<sub>2</sub> and a boron atom at the edge of BN in porous

BN/TiO<sub>2</sub> hybrid nanosheets (38 wt%) [31]. However, the position of hydroxyl O1s peak almost keeps the same position at 532.5 eV as shoulder in non-porous BN/TiO<sub>2</sub> hybrid nanosheets (38 wt%), suggesting no B—O—Ti bonds formed in non-porous hybrid nanosheets (Fig. 2f). In addition, the binding energy of 398.2 eV is a typical peak position for N 1s as shown in Fig. S6a and S6b, which is related to BN<sub>3</sub> and NB<sub>3</sub> trigonal units of BN layers [32]. Two characteristic peaks of TiO<sub>2</sub> at 456.9 eV and 462.7 eV (Fig. S6c and d) ascribe to Ti 2p<sub>3/2</sub> and Ti 2p<sub>1/2</sub> respectively.

On the basis of the above characterization results, possible formation process of B—O—Ti bonds in porous BN/TiO<sub>2</sub> hybrid nanosheets are discussed below. Since a large number of dangling bonds at pore edges of porous BNNs are not saturated and highly reactive, these dangling bonds are readily to incorporate with hydroxyl groups after the acidification by HNO<sub>3</sub>. The self-condensation in TBT (Ti(OC<sub>4</sub>H<sub>9</sub>)<sub>4</sub>) leads to the formation of Ti—O—Ti bridges and with the elimination of C<sub>4</sub>H<sub>9</sub>OH in the crystallization process of synthesized TiO<sub>2</sub> nanoparticles. When the reaction system was mixed with porous BNNs, however, positive charged Ti(VI) in TBT was loosely bounded to the surface and

pore edges of porous BNNSs which are slightly negative charged. As previously formatted B—OH was competed with Ti—O—C<sub>4</sub>H<sub>9</sub> and resulting in poly-condensation as a side-reaction. Therefore, the closely bounded small TiO<sub>2</sub> nanoparticles on porous BNNSs resulted in the formation of B—O—Ti bonds at the edge areas.

### 3.2. Photocatalytic performance of porous BN/TiO<sub>2</sub> hybrid nanosheets

The photocatalytic performances of the designed porous BN/TiO<sub>2</sub> hybrid nanosheets were evaluated by degradation of hazardous organic dyes. It is well known that organic dyes discharged from textiles, paper, plastics, tannery, and paint industries are considered as the primary pollutants in water sources [33]. Here, organic dye, rhodamine B, was selected as a model organic pollutant to evaluate the photocatalytic performance of porous BN/TiO<sub>2</sub> hybrid nanosheets under both solar and visible light irradiation. Fig. S7a shows time-dependent photocatalytic activities of synthesized TiO<sub>2</sub> nanoparticles, P25 and porous and non-porous BN/TiO<sub>2</sub> hybrid nanosheets with different TiO<sub>2</sub> loading under simulated solar light.

Before light irradiation, the suspension samples and RhB were stirred in dark for 1 h to achieve the adsorption/desorption equilibrium between dye and photocatalysts. It is noted that all the porous BN/TiO<sub>2</sub> hybrid nanosheets exhibit adsorption intensity (about 6%) to the RhB during the period, compared with synthesized TiO<sub>2</sub> nanoparticles and P25, which attributed the strong adsorption capacity of porous BNNSs with a large specific surface area. Under the radiation of a simulated solar light, P25 exhibits a little higher photocatalytic activity than the synthesized TiO<sub>2</sub> nanoparticles due to the special electronic states of two crystal structures (anatase and rutile) in P25 acting as a semiconductor–semiconductor junction [34]. However, all the three porous BN/TiO<sub>2</sub> hybrid nanosheets display significantly improved photodegradation efficiencies to RhB compared with P25. The highest photocatalytic activity of porous BN/TiO<sub>2</sub> hybrid nanosheets was obtained from the porous BN/TiO<sub>2</sub> hybrid nanosheets (38 wt%), achieving a degradation percentage up to 99% within 6 h, which is much higher than that of P25 (~60%) as shown in Fig. 3a. When non-porous BN/TiO<sub>2</sub> hybrid nanosheets (38 wt%) were tested under the same conditions, the degradation percentage was only up to 67% within 6 h (Fig. S7a). The results further demonstrated that the porous structure plays an important role in enhancing degradation performance. The insufficient loading of TiO<sub>2</sub> (18 wt%) into porous BN/TiO<sub>2</sub> hybrid nanosheets may induce the decrease of photon harvest of TiO<sub>2</sub> particles under light irradiation, while excessive loading of TiO<sub>2</sub> (51 wt%) may block the photo-electrons transfer between TiO<sub>2</sub> particles and porous BN nanosheets. These results indicated that porous BN/TiO<sub>2</sub> (38 wt%) hybrid nanosheets are a good photocatalyst with high photocatalytic activity.

As the UV accounts for only ~4% of the total solar radiation energy, it's desired to design visible-light-driven photocatalysts [35,36]. Here, the porous BN/TiO<sub>2</sub> hybrid nanosheets (38 wt%) still display high degradation percentage up to 99% to RhB under the visible light irradiation ( $\lambda > 420$  nm), as shown in Figs. 3 b and S8. It has been approved that both de-ethylation and degradation of RhB take place in the presence of TiO<sub>2</sub> particles under visible light irradiation [37]. The whole process was stepwise photocatalytic decomposition. Similar result was obtained in this study, specifically, the characteristic absorption peak of RhB at 554 nm, decreased gradually during the irradiation, suggesting the successful degradation of RhB, as shown in Fig. 3(c). The peak also showed a hypsochromic shift from 554 nm to 498 nm, which corresponded to a step-by-step deethylation to give *N,N,N'*-triethyl rhodamine (TER, 539 nm), *N,N*'-diethyl rhodamine (DER, 522 nm), *N*-ethyl rhodamine (MER, 510 nm), and rhodamine at 498 nm [38]. Concurrently, the absorbance peaks rapidly faded away, and dis-

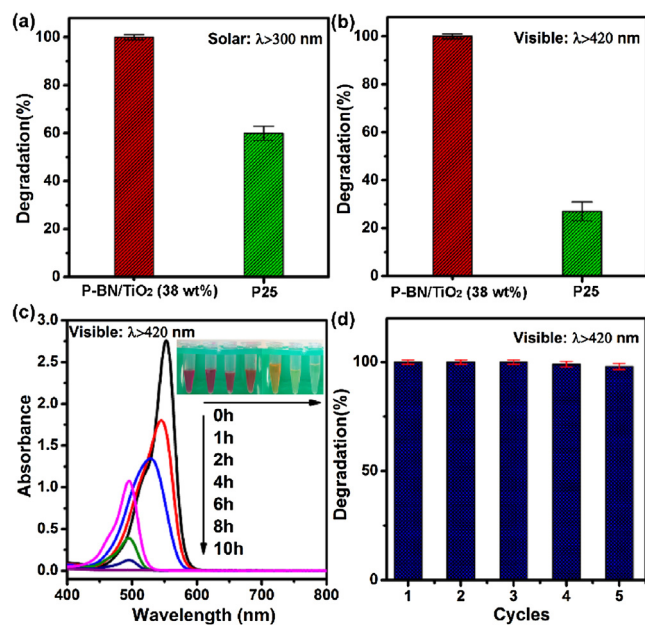


**Fig. 3.** Photodegradation of Rhodamine B (RhB) under different irradiation conditions: (a) solar light irradiation  $\lambda > 300$  nm, and (b) visible light  $\lambda > 420$  nm by P25 and porous BN/TiO<sub>2</sub> hybrid nanosheets (38 wt%). (c) Visible absorbance spectra of the RhB solution with the porous BN/TiO<sub>2</sub> hybrid nanosheets (38 wt%) under visible light irradiation. The inset shows the photographs of the RhB solutions after different irradiation time. (d) The degradation performance of RhB of porous BN/TiO<sub>2</sub> hybrid nanosheets (38 wt%) under visible light with 5 successive cycles.

appeared after 10 h of photodegradation by porous BN/TiO<sub>2</sub> hybrid nanosheets (38 wt%) (Fig. 3c) [38]. The photographs of the RhB solutions show the color changing from pink to clear with increasing visible light irradiation time as inserted in Fig. 3c, further confirming the full photodegradation of RhB. Importantly, the porous BN/TiO<sub>2</sub> hybrid nanosheets (38 wt%) maintained high photocatalytic activity (97%) even after 5 cycles, as shown in Fig. 3d. In contrast, the RhB degradation by P25 was negligible. This degradation is caused by the dye-sensitization mechanism, given that P25 is well-known not to absorb visible light [39,40]. To rule out this dye-sensitization effect in porous BN/TiO<sub>2</sub> hybrid nanosheets (38 wt%) and demonstrate that it was their photocatalytic activity under visible light responsible for the RhB degradation, these hybrid nanosheets were applied to degrade the phenol. It should be noted that no phenol degradation with TiO<sub>2</sub> could be observed under the yellow lamp (wavelength: 480–720 nm), with which would be the only operational pathway for a dye-sensitization process to be active [39]. In this regard, phenol became the highly-recommended substrate for the test of the photocatalytic activity of new materials in visible light [39]. Previous studies revealed that the products at the initial stage of reaction include hydroquinone, pyrocatechol, 1,2,4-benzenetriol, pyrogallol, and 2-hydroxy-1,4-benzoquinone. These intermediates were finally completely mineralized to CO<sub>2</sub> and H<sub>2</sub>O by photo-oxidation in the presence of TiO<sub>2</sub> [41,42]. It can be seen from Fig. S9 that after irradiating the phenol solution for a certain period, around 83% of phenol could be degraded by porous BN/TiO<sub>2</sub> hybrid nanosheets (38 wt%). The phenol degradation was confirmed with the UV-vis absorbance spectra of the phenol solution during the visible light irradiation process, in which the characteristic adsorption peak at 269 nm decreased gradually (Fig. S9b). However, only 13% of the phenol was degraded by P25 in the same condition (Fig. S9b). The superior photocatalytic activity of porous BN/TiO<sub>2</sub> hybrid nanosheets (38 wt%) to that of P25 for both RhB and phenol degradation in visible light irradiation firmly

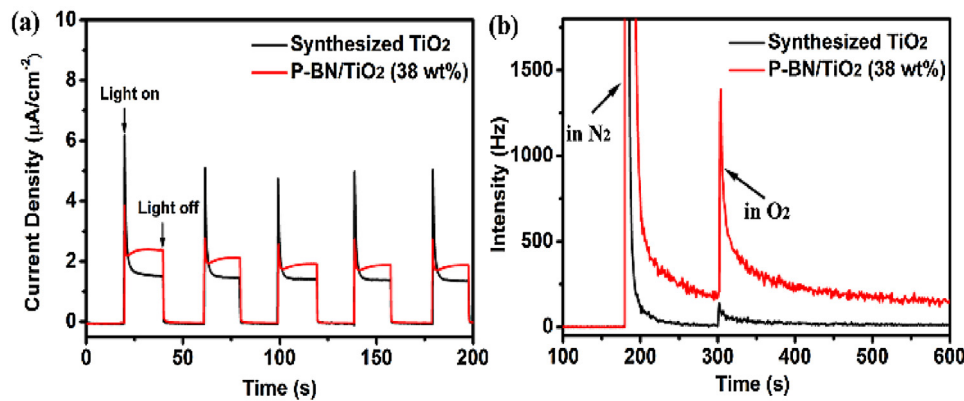


**Fig. 4.** (a) Photocurrent responses of synthesized  $\text{TiO}_2$  and porous  $\text{BN}/\text{TiO}_2$  hybrid nanosheets (38 wt%) under solar light irradiation. The applied potential is 0 V vs.  $\text{Ag}/\text{AgCl}$ . (b) Emission profiles from photo-induced chemiluminescence experiments for synthesized  $\text{TiO}_2$  and porous  $\text{BN}/\text{TiO}_2$  hybrid nanosheets (38 wt%) by using light wavelengths range from 320 to 500 nm.

demonstrated their visible-light-driven characteristic, presenting the great potentials of these novel hybrid nanosheets.

### 3.3. Mechanism of the improved photocatalytic activity of porous $\text{BN}/\text{TiO}_2$ hybrid nanosheets (38 wt%)

The improved photocatalytic activity of porous  $\text{BN}/\text{TiO}_2$  hybrid nanosheets for hazardous organic dyes (RhB) benefits from the high BET surface area of porous BNNSs firstly. It is essential to distribute  $\text{TiO}_2$  nanoparticles evenly on the surface of porous BNNSs, which can prevent  $\text{TiO}_2$  nanoparticle aggregation during the recycling process and prompt the adsorption of adsorbents, so that to accelerate the photocatalysis reaction and keep excellent cyclability [19]. This high BET surface area of porous  $\text{BN}/\text{TiO}_2$  hybrid nanosheets also enabled their high adsorption ability for the RhB. Specifically, 6% RhB was adsorbed on porous  $\text{BN}/\text{TiO}_2$  hybrid nanosheets (38 wt%) after being stirred in the dark condition for 1 h, while no RhB was adsorbed on P25 and synthesized  $\text{TiO}_2$  (Fig. S7). It is vital to increase adsorption ability of a photocatalyst as photo-induced reaction species are dominantly located on its surfaces. Given that  $\text{TiO}_2$  nanoparticles were uniformly anchored on porous BNNSs, adsorption of RhB on porous BNNSs increased the approach of pollutants on loaded  $\text{TiO}_2$  nanoparticles, thus increasing the photo reaction rates. During the photocatalytic processes, the adsorbed RhB was gradually degraded, leaving vacancies for the further RhB adsorption, thus maintaining adsorption equilibrium and promoting the RhB degradation. Another important contributing factor is the conjugate structure change caused by the formation of new actively chemical bonding specie  $\text{B}=\text{O}-\text{Ti}$  at the open edges of pores on porous BNNSs. The formation of  $\text{B}=\text{O}-\text{Ti}$  bonds during the synthesis processes caused the energy rearrangement, which lead to the narrowed band gap of porous  $\text{BN}/\text{TiO}_2$  hybrid nanosheets (38 wt%) and thus induced the excited wavelength extending from UV light region to visible light region. These novel photocatalysts were therefore endowed with highly efficient visible-light-driven characteristic.

On the other side, the  $\text{B}=\text{O}-\text{Ti}$  bonds provide a condition for the photogenerated electrons from conduction band of  $\text{TiO}_2$  nanoparticles transfer to porous BNNSs easily. As the generated electrons can be delocalized in the huge  $\pi-\pi$  conjugate system of porous BNNSs, the recombination rate of electron-hole pair would be retarded and thus contributed to the improvement of photocatalytic activity of  $\text{TiO}_2$ . The photocurrent spectroscopy was used to detect transient photocurrent response and to provide evidence for the electron-hole transfer mechanism [43]. The typical photocurrent ( $I$ ) and time ( $t$ ) response curves for both synthesized  $\text{TiO}_2$  and porous  $\text{BN}/\text{TiO}_2$

hybrid nanosheets (38 wt%) with several switch-on/off cycles under solar light irradiation are shown in Fig. 4a. A higher photocurrent was obtained from the porous  $\text{BN}/\text{TiO}_2$  hybrid nanosheets (38 wt%) compared with the synthesized  $\text{TiO}_2$ , which indicates more efficient separation of photo generated electrons or holes and less recombination of the charge carrier at the interface between porous BNNSs and  $\text{TiO}_2$ . In addition, photo-induced chemiluminescent emission can detect the concentration of free radicals on the surface resulting from the recombination of photo induced charge transportation of sample [44]. Therefore, photo-induced chemiluminescent emission spectra is another powerful demonstration of enhanced charge transportation and separation properties, as shown in Fig. 4b. From the photo-induced chemiluminescent emission spectra, we can see that a sharp intense emission ( $\sim 1388$  Hz) is observed in porous  $\text{BN}/\text{TiO}_2$  hybrid nanosheets (38 wt%) after the immediately admission of oxygen, which is approximately 10 times higher than the intensity of synthesized  $\text{TiO}_2$  ( $\sim 135$  Hz), further reveals effective separation of photo induced electron and hole resulting from the formation of new  $\text{B}=\text{O}-\text{Ti}$  bonds between porous BNNSs and  $\text{TiO}_2$ .

## 4. Conclusion

We demonstrate that, for the first time, porous  $\text{BN}/\text{TiO}_2$  hybrid nanosheets with new actively chemical bonding specie  $\text{B}=\text{O}-\text{Ti}$  were successfully prepared using a solvothermal process. This exotic specie benefits from the richly exposed edges of pores and edges of the unique porous BNNS structures, which endow the hybrid material with capability being responsive to both UV and visible lights. As expected, the hybrid material, especially for the porous  $\text{BN}/\text{TiO}_2$  hybrid nanosheets (38 wt%), shows the optimal photocatalytic activities (up to 99%) for degradation of hazardous organic dye (rhodamine B) under visible light. The successful phenol degradation with porous  $\text{BN}/\text{TiO}_2$  hybrid nanosheets (38 wt%) further demonstrated their visible-light-driven characteristic. This work develops a new multifunctional porous  $\text{BN}/\text{TiO}_2$  hybrid nanosheets as photocatalysts under visible light irradiation, and also opens a new doorway to guide further design of advanced hybrid photocatalysts with highly efficient visible-light-driven characteristic.

## Acknowledgements

Financial support from the Australian Research Council Discovery Early Career Researcher Award scheme (DE150101617 and DE140100716), the National Natural Science Foundation of China

(NSFC 51302197) and Deakin University, Central Research Grant Scheme are acknowledged.

## Appendix A. Supplementary data

Supplementary data associated with this article can be found, in the online version, at <http://dx.doi.org/10.1016/j.apcatb.2017.02.011>.

## References

- [1] N. Pinna, G. Neri, M. Antonietti, M. Niederberger, *Angew. Chem.* 43 (2004) 4345–4349.
- [2] P. Innocenzi, L. Malfatti, G.J.A.A. Soler-Illia, *Chem. Mater.* 23 (2011) 2501–2509.
- [3] K.R. Prasad, K. Koga, N. Miura, *Chem. Mater.* 16 (2004) 1845–1847.
- [4] W.W. Lei, D. Portehault, D. Liu, S. Qin, Y. Chen, *Nat. Commun.* 4 (2013) 1777.
- [5] Q. Liu, L. Jiang, L. Guo, *Small* 10 (2014) 48–51.
- [6] L. Gao, Z. Cheng, Q. Xiang, Y. Zhang, J. Xu, *Sens. Actuators B: Chem.* 208 (2015) 436–443.
- [7] S. Han, D. Wu, S. Li, F. Zhang, X. Feng, *Adv. Mater.* 26 (2014) 849–864.
- [8] J. Dai, X. Wu, J. Yang, X.C. Zeng, *J. Phys. Chem. Lett.* 5 (2014) 393–398.
- [9] N.G. Shang, P. Papakonstantinou, M. McMullan, M. Chu, *Adv. Funct. Mater.* 18 (2008) 3506–3514.
- [10] C. Su, M. Acik, K. Takai, J. Lu, S.J. Hao, Y. Zheng, P. Wu, Q. Bao, T. Enoki, Y.J. Chabal, K.P. Loh, *Nat. Commun.* 3 (2012) 1298.
- [11] W.W. Lei, D. Liu, Y. Chen, *Adv. Mater. Interfaces* 2 (2015) 1400529.
- [12] C. Zhi, Y. Bando, C. Tang, H. Kuwahara, D. Golberg, *Adv. Mater.* 21 (2009) 2889–2893.
- [13] W.W. Lei, V.N. Mochalin, D. Liu, S. Qin, Y. Gogotsi, Y. Chen, *Nat. Commun.* 6 (2015) 8849.
- [14] C.-A. Lin, J.C.S. Wu, J.-W. Pan, C.-T. Yeh, *J. Catal.* 210 (2002) 39–45.
- [15] C.J.H. Jacobsen, *J. Catal.* 200 (2001) 1–3.
- [16] G. Postole, M. Calderaru, N.I. Ionescu, B. Bonnetot, A. Auroux, C. Guimon, *Thermochim. Acta* 434 (2005) 150–157.
- [17] C. Tang, J. Li, Y. Bando, C. Zhi, D. Golberg, *Chem.–Asian J.* 5 (2010) 1220–1224.
- [18] M. Wang, M. Li, L. Xu, L. Wang, Z. Ju, G. Li, Y. Qian, *Catal. Sci. Technol.* 1 (2011) 1159–1165.
- [19] Y. Ide, F. Liu, J. Zhang, N. Kawamoto, K. Komaguchi, Y. Bando, D. Golberg, *J. Mater. Chem. A* 2 (2014) 4150–4155.
- [20] Q. Weng, Y. Ide, X. Wang, X. Wang, C. Zhang, X. Jiang, Y. Xue, P. Dai, D. Golberg, *Nano Energy* 16 (2015) 19.
- [21] Q. Weng, X. Wang, C. Zhi, Y. Bando, D. Golberg, *ACS Nano* 2 (2013) 1558–1565.
- [22] W. Lei, H. Zhang, Y. Wu, B. Zhang, D. Liu, S. Qin, Z. Liu, L. Liu, Y. Ma, Y. Chen, *Nano Energy* 6 (2014) 219–224.
- [23] D. Liu, L. He, W.W. Lei, K.D. Klika, L. Kong, Y. Chen, *Adv. Mater. Interfaces* 2 (2015) 1500228.
- [24] W. Xie, M. Zhang, D. Liu, W. Lei, L. Sun, X. Wang, *J. Photochem. Photobiol. A: Chem.* 333 (2017) 165–173.
- [25] D. Liu, M.W. Zhang, W.J. Xie, L. Sun, Y. Chen, W.W. Lei, *Catal. Sci. Technol.* 6 (2016) 8309–8313.
- [26] W. Xie, M. Zhang, D. Liu, W. Lei, L. Sun, X. Wang, *ACS Sustain. Chem. Eng.* (2016), <http://dx.doi.org/10.1021/acssuschemeng.6b01896>.
- [27] A. Nag, K. Raidongia, K.P.S.S. Hembram, R. Datta, U.V. Waghmare, C.N.R. Rao, *ACS Nano* 4 (2010) 1539–1544.
- [28] D. Reyes-Coronado, G. Rodriguez-Gattorno, M.E. Espinosa-Pesqueira, C. Cab, R. Coss, G. Oskam, *Nanotechnology* 19 (2008) 145605.
- [29] Y. Hau NG, I.V. Lightcap, K. Goodwin, M. Matsumura, P.V. Kamat, *J. Phys. Chem. Lett.* 1 (2010) 2222–2227.
- [30] D. Chen, D. Yang, Q. Wang, Z. Jiang, *Ind. Eng. Chem. Res.* 45 (2006) 4110–4116.
- [31] W. Zhang, T. Hu, B. Yang, P. Sun, H. He, *J. Adv. Oxid. Technol.* 16 (2013) 261–267.
- [32] D. Liu, W. Lei, S. Qin, Y. Chen, *Sci. Rep.* 4 (2014) 4453.
- [33] G. Crini, *Bioresour. Technol.* 97 (2006) 1061–1085.
- [34] K. Woan, G. Pyrgiotakis, W. Sigmund, *Adv. Mater.* 21 (2009) 2233–2239.
- [35] M. Zhu, C. Zhai, L. Qiu, A.S. Pation, Y. Du, M.C. Goh, *ASC Sustain. Chem. Eng.* 3 (2015) 3123–3129.
- [36] C. Zhai, M. Zhu, F. Pang, D. Bin, C. Lu, M.C. Goh, P. Yang, Y. Du, *ACS Appl. Mater. Interfaces* 8 (2016) 5927–5980.
- [37] T. Wu, G. Liu, J. Zhao, H. Hidaka, N. Serpone, *J. Phys. Chem. B* 102 (1998) 5845–5851.
- [38] J. Zhang, W. Dai, Q. Tian, Z. Li, L. Xie, J. Wang, P. Liu, *Langmuir* 12 (2010) 9686–9694.
- [39] N. Barbero, D. Vione, *Environ. Sci. Technol.* 50 (2016) 2130–2131.
- [40] H. Kyung, J. Lee, W. Choi, *Environ. Sci. Technol.* 39 (39) (2005) 2376–2382.
- [41] K.I. Okamoto, Y. Yamamoto, H. Tanaka, M. Tanaka, A. Itaya, *Bull. Chem. Soc. Jpn.* 58 (1985) 2015–2022.
- [42] J. Tseng, C.P. Huang, *ACS Symp. Ser.* 422 (1990) 12–39.
- [43] N. Wu, H. Wei, L. Zhang, *Environ. Sci. Technol.* 46 (2012) 419–425.
- [44] K.K. Manga, Y. Zhou, Y. Yan, K.P. Loh, *Adv. Funct. Mater.* 19 (2009) 3638–3643.